

Enhanced transport of spin-orbit-coupled Bose gases in disordered potentialsY. Yue¹, C. A. R. Sá de Melo,² and I. B. Spielman¹¹*Joint Quantum Institute, National Institute of Standards and Technology, and University of Maryland, Gaithersburg, Maryland 20899, USA*²*School of Physics, Georgia Institute of Technology, Atlanta, Georgia 30332, USA*

(Received 4 July 2020; accepted 28 August 2020; published 17 September 2020)

Anderson localization is a single-particle localization phenomena in disordered media that is accompanied by an absence of diffusion. Spin-orbit coupling (SOC) describes an interaction between a particle's spin and its momentum that directly affects its energy dispersion, for example, creating dispersion relations with gaps and multiple local minima. We show theoretically that combining one-dimensional spin-orbit coupling with a transverse Zeeman field suppresses the effects of disorder, thereby increasing the localization length and conductivity. This increase results from a suppression of backscattering between states in the gap of the SOC dispersion relation. Here, we focus specifically on the interplay of disorder from an optical speckle potential and SOC generated by two-photon Raman processes in quasi-one-dimensional Bose-Einstein condensates. We first describe backscattering by using a Fermi golden rule approach, and then numerically confirm this picture by solving the time-dependent one-dimensional Gross-Pitaevskii equation for a weakly interacting Bose-Einstein condensate with SOC and disorder. We find that on the tens of millisecond timescale of typical cold atom experiments moving in harmonic traps, initial states with momentum in the zero-momentum SOC gap evolve with negligible backscattering, while without SOC these same states rapidly localize.

DOI: [10.1103/PhysRevA.102.033325](https://doi.org/10.1103/PhysRevA.102.033325)**I. INTRODUCTION**

Anderson localization (AL), introduced in 1958 [1], describes the localization of waves in disordered media. Anderson studied the evolution of a wave packet undergoing multiple-scattering processes from a random potential and proved that the scattered waves can constructively interfere, leading to localization. This general starting point makes AL applicable to many systems, including optical waves in disordered media [2–4], electrons in imperfect crystals [1], and matter waves in disordered optical potentials [5–7]. In materials, microscopic electron-scattering processes partly govern the macroscopic conductivity, and AL predicts a metal-insulator transition. Increasing a system's conductivity therefore requires some change in these scattering processes. The most straightforward mechanism is to reduce the disorder strength. Here we describe an alternate approach in which spin-orbit coupling (SOC) greatly suppresses the backscattering and thereby increases the conductivity. We then propose a realization of this effect that uses a cold-atom Bose-Einstein condensate (BEC) with laser-induced SOC [8] and disorder from optical speckle.

SOC is a ubiquitous phenomenon in physical systems that describes the interaction between a particle's spin and its momentum. When SOC is combined with a transverse magnetic field (in the sense of Zeeman shifts, not Lorentz forces), gaps in the dispersion relation can open at spin-degeneracy points. The opening of these gaps modifies the electrons' scattering processes and affects transport. AL was first realized for ultracold atomic systems [6,7] in 2008, and the experimental techniques are now well established. Shortly thereafter, techniques for creating SOC in the cold atom laboratory were

demonstrated [8]. Together, this makes cold-atom systems an ideal platform to study the interplay between AL and SOC.

Optical speckle is a powerful tool for creating disordered potentials for atomic systems [9,10]. The strength of the resultant potential is under direct experimental control: the spatial correlation length is tunable and the correlation function is well known. Here we analytically and numerically study backscattering in speckle potentials of quasi-one-dimensional (quasi-1D) spin-orbit-coupled BECs (SOBECs) and compare with the case without SOC. We show that SOC can reduce the scattering processes for specific momentum states. In the broader context, our results suggest that, in thin nanowires, SOC might significantly decrease resistance and improve energy efficiency in electronic devices.

This paper is organized as follows: In Sec. II, we begin with an introduction to optical speckle as it pertains to our proposal. In Sec. II, we analytically calculate the probability an initial momentum state being scattered by the speckle potential to any final momentum state and show that SOC can reduce backscattering. Lastly, in Sec. III, we describe numerical simulations of quasi-1D BECs starting in different momentum states subject to a speckle potential with and without SOC. We show that even with the higher-order scattering processes and interaction between particles present in the numerical simulations, SOC can reduce the localization effects of disorder and enhance transport.

II. CHARACTERISTICS OF OPTICAL SPECKLE

Optical speckle can be understood as the self-interfering wave field of a laser after acquiring random phase by reflection off rough surfaces or transmission through disordered

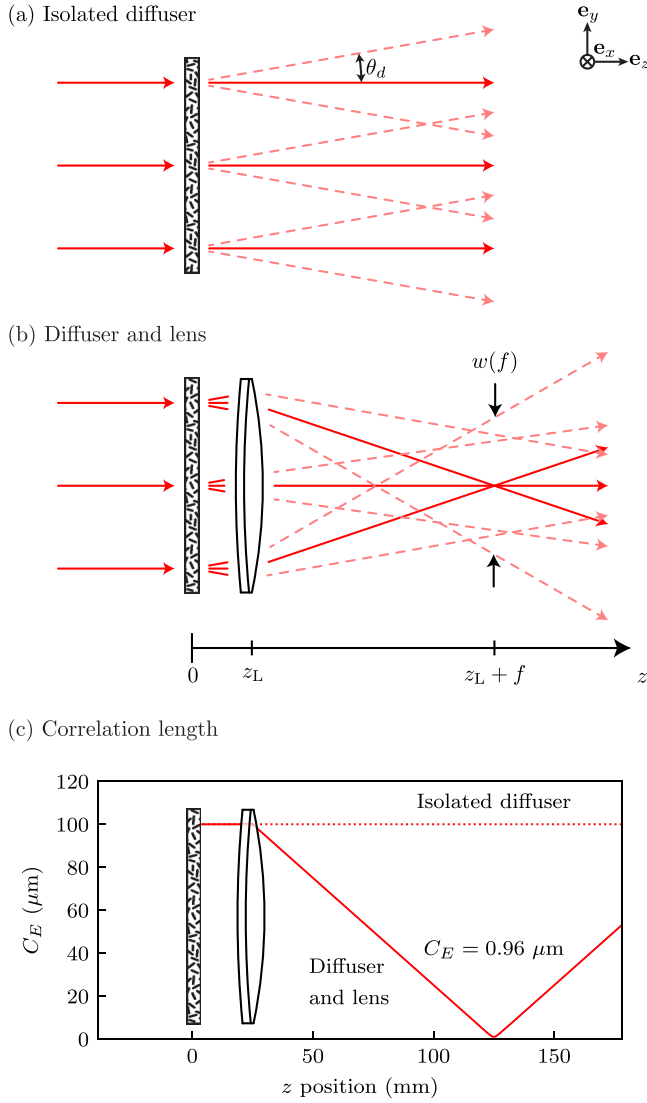


FIG. 1. Optical speckle schematic. (a) A collimated beam is transmitted through a rough medium and its intensity is measured in plane z . (b) The diverged beam after the rough medium is imaged by a lens at plane $z = z_L$ and f is the focal point of the lens. (c) Field-field correlation length for a Gaussian speckle beam initially with $\sigma = 100 \mu\text{m}$ and $w = 25 \text{ mm}$ as a function of propagation distance. The red curves plot $C_E(z)$ computed with (solid) and without (dashed) a lens with focal length $f = 100 \text{ mm}$ at $z_L = 25 \text{ mm}$.

media, called a diffuser [11]. We focus on the transmission case and assume that the spatial scale of the disorder σ is small in comparison with the laser beam size and that the diffuser transmits light uniformly. The transmitted field can be intuitively thought of as many waves scattered from microscopic elements comprising the diffuser, so randomness arises. As a disordered field, optical speckle is characterized by its intensity distribution, spatial intensity correlation function, and power spectral density (PSD).

As Fig. 1 shows, ray optics in the paraxial limit provides a simple and useful approach to estimating the on-axis beam properties of a speckle beam a distance z beyond a diffuser. As a collimated laser beam of wavelength λ travels through a

diffuser of diameter D_d , it acquires a local divergence angle $\theta_d \simeq \lambda/(2\sigma)$.

Figure 1(a) depicts the simplest case consisting of an isolated diffuser, for which there are two qualitatively different regimes: A near-field regime with $z < D_d/(2\theta_d)$, where the typical length scale of optical speckle is σ , and a far-field regime where the numerical aperture (NA) of the diffuser increases the speckle scale to $(\lambda/2)(2z/D_d)$. This simple approach is insufficient because we are interested in micrometer-scale speckle, which is far smaller than the 10 to 100 micrometer scale of σ for commercial diffusers.

In Fig. 1(b) we add a lens with diameter D_L and focal length f just after the diffuser. In the focal plane of the lens, the speckle scale is set by the lens NA, giving a speckle length scale $\lambda f/D_L$ independent of σ . In contrast, the beam width at the focal plane $w(f) \simeq 2f\theta_d$ is set by the speckle scale σ and not the lens diameter.

In the following section we derive the origin of these design guidelines from the paraxial wave equation.

A. Gaussian beam equations with speckle

We focus on monochromatic optical electric fields $E(\mathbf{x}, t)$ with angular frequency ω traveling predominantly along \mathbf{e}_z . Such waves can be decomposed as $E(\mathbf{x}, t) = E_\perp(\mathbf{r}; z) \exp[i(k_0 z - \omega t)]$, where $E_\perp(\mathbf{r}; z)$ describes the transverse structure of the electric field with the high spatial frequencies associated with the nominal propagation along \mathbf{e}_z factored out. For spatial scales in excess of the optical wavelength, the transverse field obeys the paraxial wave equation

$$-2ik_0 \partial_z E_\perp(\mathbf{r}; z) = [-\nabla_\perp^2 + k_0^2 \chi(\mathbf{r}; z)] E_\perp(\mathbf{r}; z) \quad (1)$$

traveling in a material with relative susceptibility $\chi(\mathbf{r}; z)$. We suppress the \perp subscript in the remainder of our discussion.

Upon traversing through a thin but disordered material with susceptibility $\chi(\mathbf{r})$ and thickness δz , an initially Gaussian wave field $E^-(\mathbf{r}, 0) = E_0 \exp\{-\mathbf{r}^2/w^2\}$ acquires a position-dependent complex phase $\phi(\mathbf{r}) = \chi(\mathbf{r})k_0 \delta z/2$. The resultant field

$$E^+(\mathbf{r}, 0) = E^-(\mathbf{r}, 0) \exp[-i\phi(\mathbf{r})] \quad (2)$$

carries the imprint of the disordered medium. The field a distance z beyond the speckle plate follows from

$$E(\mathbf{r}; z) = \frac{-ik_0}{2\pi z} \int d^2 \mathbf{r}' E^+(\mathbf{r}'; 0) e^{-ik_0 |\mathbf{r} - \mathbf{r}'|^2 / 2z}, \quad (3)$$

which is the formal solution to the paraxial wave equation (1). We model typical diffusion plates, for which (a) the correlation function of the susceptibility, $\langle \chi(\mathbf{r}_1) \chi(\mathbf{r}_2) \rangle$, depends only on relative distance $|\mathbf{r}_1 - \mathbf{r}_2|$, where $\langle \dots \rangle$ denotes the ensemble average over disorder realizations; (b) the variation of the imprinted phase $\phi(\mathbf{r})$ is much larger than 2π with

$$\langle \exp[-i\phi(\mathbf{r}_1)] \rangle = 0, \quad (4)$$

i.e., $\phi(\mathbf{r})$ is uniformly distributed over the interval $[-\pi, \pi]$.

We turn to the field-field correlation function

$$C_E(\mathbf{r}_1, \mathbf{r}_2; z) = \langle E(\mathbf{r}_1; z) E^*(\mathbf{r}_2; z) \rangle - \langle E(\mathbf{r}_1; z) \rangle \langle E^*(\mathbf{r}_2; z) \rangle \quad (5)$$

to characterize the statistical properties of the disordered electric field. Equation (4) implies that the second term is zero. At $z = 0$, the uniform phase distribution implies $\langle E^+(\mathbf{r}; 0) \rangle = 0$, giving

$$\frac{C_E(\mathbf{r}_1, \mathbf{r}_2; 0)}{E_0^2} = \exp\left(-\frac{\mathbf{r}_1^2 + \mathbf{r}_2^2}{w^2}\right) \langle \exp\{-i[\phi(\mathbf{r}_1) - \phi(\mathbf{r}_2)]\} \rangle.$$

Under the assumptions of the typical diffusion plates, we model the phase-phase correlation function

$$\langle \exp\{-i[\phi(\mathbf{r}_1) - \phi(\mathbf{r}_2)]\} \rangle = \exp\left(-\frac{|\mathbf{r}_1 - \mathbf{r}_2|^2}{\sigma^2}\right), \quad (6)$$

with a Gaussian decay of width σ that is amenable to the following analytic treatments. The relation

$$\langle \exp\{-i[\phi(\mathbf{r}_1) + \phi(\mathbf{r}_2)]\} \rangle = 0, \quad (7)$$

which follows from Eq. (4), in conjunction with the assumption that the correlation function depends only on relative distance, is useful as well.

We first consider the case illustrated by Fig. 1(a) where a Gaussian beam goes through a large disordered medium. The field-field correlation function at all positions following the disordered medium can be exactly computed and takes the form

$$\begin{aligned} \frac{C_E(\mathbf{r}_1, \mathbf{r}_2; z)}{E_0^2} &= \left[\frac{w}{w(z)}\right]^2 \exp\left(-ik_0 \frac{\mathbf{r}_1^2 - \mathbf{r}_2^2}{2R(z)}\right) \\ &\times \exp\left(-\frac{\mathbf{r}_1^2 + \mathbf{r}_2^2}{w^2(z)}\right) \exp\left(-\frac{|\mathbf{r}_1 - \mathbf{r}_2|^2}{\sigma^2(z)}\right), \end{aligned} \quad (8)$$

reminiscent of that of Gaussian beams.

This correlation function is characterized in terms of three z -dependent functions: the beam waist $w(z)$, the radius of curvature $R(z)$, and the correlation length $\sigma(z)$. Each of these is simply related to a reduced Rayleigh range $z_R^* = z_R/M$, with conventional Rayleigh range $z_R = k_0 w^2/2$ and beam quality factor $M^2 = 1 + 2w^2/\sigma^2$. The resulting coefficients

$$\left[\frac{w(z)}{w}\right]^2 = \left[\frac{\sigma(z)}{\sigma}\right]^2 = 1 + \left(\frac{z - z_0}{z_R^*}\right)^2 \quad (9)$$

and

$$\frac{R(z)}{z - z_0} = 1 + \left(\frac{z_R^*}{z - z_0}\right)^2 \quad (10)$$

take the same form as a usual Gaussian beams focused at z_0 . Lastly, as in Fig. 1(b), an ideal lens with focal length f at position z_L gives new Gaussian beam parameters defined by

$$\frac{w'}{w} = \frac{\sigma'}{\sigma} = f[(z'_0 - z_L - f)^2 + z_R^{*2}]^{-1/2} \quad (11)$$

and

$$(z'_0 - z_L)^{-1} = f^{-1} - \left[(z_L - z_0) + \frac{z_R^{*2}}{z_L - z_0 - f} \right]^{-1},$$

where the first expression defines the magnification and the second is analogous to the usual lens maker's equation [12]. While this leaves M^2 unchanged, the Rayleigh range is altered owing to the change in w . Altogether these relations fully

define the field-field correlation function C_E throughout an ideal imaging system.

In most quantum-gas experiments, optical potentials are created by using laser light in the far-detuned limit, thereby experiencing a potential proportional to the optical intensity

$$I(\mathbf{r}; z) = \frac{c\epsilon_0}{2} |E(\mathbf{r}; z)|^2, \quad (12)$$

not the electric field directly. The ensemble-averaged intensity

$$\langle I(\mathbf{r}; z) \rangle = \frac{c\epsilon_0}{2} C_E(\mathbf{r}, \mathbf{r}; z), \quad (13)$$

simply related to the field-field correlation function (8), contains no information about the optical speckle except for the changed M^2 .

As discussed in the next section, the power spectral density (PSD) of the intensity,

$$\begin{aligned} \rho(\mathbf{k}; z) &= \langle \tilde{I}(\mathbf{k}; z) \tilde{I}^*(\mathbf{k}; z) \rangle \\ &= \frac{\pi^2 w^2(z)}{4M^2} \exp\left\{-\frac{\mathbf{k}^2 w^2(z)}{4M^2}\right\}, \end{aligned} \quad (14)$$

computed by using Eq. (8), describes the momentum-change imparted by the speckle potential to a moving atomic wave packet.

B. Correlation length

The field-field correlation length

$$c_E^2(z) = \frac{\iint |C_E(\mathbf{r}_1, \mathbf{r}_2; z)| |\mathbf{r}_1 - \mathbf{r}_2|^2 d^2\mathbf{r}_1 d^2\mathbf{r}_2}{\iint |C_E(\mathbf{r}_1, \mathbf{r}_2; z)| d^2\mathbf{r}_1 d^2\mathbf{r}_2} \quad (15)$$

$$= \frac{2w^2(z)\sigma^2(z)}{2w^2(z) + \sigma^2(z)} \approx \sigma^2(z) \quad (16)$$

obtained from Eq. (8) sets the scale over which the electric field retains its spatial coherence. The field-field correlation length is minimized at $z = z_0$ and is always larger than σ . Generally, speckle beams operate in the regime $w \gg \sigma$, where there are many speckle grains within a large beam, giving the final approximate relation.

As was already noted in our ray-optics discussion, this has important implications for experiment design. For cold atom experiments such as ours, the large momentum change imparted by short-length-scale speckle is essential, where a correlation length at or below the micron scale is desirable. Since the correlation length available for typical commercial diffusers ranges from 10 to 100 μm , an additional focusing stage is required.

A focusing lens can easily take the 10 to 100 μm correlation length available for typical commercial diffusers and create a beam with submicrometer correlation length at its focus. Figure 1(c) compares the correlation length of a beam with (red solid) and without (red dashed) a focusing lens for the specific case of an initial laser beam of wavelength $\lambda = 532$ nm with input Gaussian beam parameters: focal point $z_0 = 0$, beam waist $w = 25$ mm, and correlation length $\sigma = 100$ μm . This beam is focused by a lens of focal length $f = 100$ mm, the correlation length at the focus is $c_E = 0.96$ μm . The remaining derived beam parameters are $M^2 \approx 1.25 \times 10^5$, $z_R \approx 3.7$ km, and $z_R^* \approx 10.4$ m.

C. Impact of apertures

In the case of focusing optical speckle as shown in Fig. 1(b), a lens of focal length f and diameter $D_L \ll w$ is placed at $z = z_L \leq k_0 \sigma^2$. The field in the plane $z = z_L$ before the lens, $E^-(\mathbf{r}; z_L)$ is essentially unchanged from field $E^+(\mathbf{r}; 0)$. The field $E^-(\mathbf{r}; z_L)$ passes through the lens aperture, where it acquires a position-dependent phase and is truncated outside the lens. The emerging field $E^+(\mathbf{r}; z_L)$ propagates to the focal plane $z = f + z_L$ where it is

$$E_f(\mathbf{r}) = \frac{-ik_0}{2\pi f} e^{-ik_0 r^2/2f} \int_{|\mathbf{r}'| < \frac{D_L}{2}} d^2 \mathbf{r}' E^+(\mathbf{r}'; 0) e^{ik_0 \mathbf{r} \cdot \mathbf{r}'/f}. \quad (17)$$

When $\sigma \ll D_L \ll w$, the field-field correlation function at the focal plane is

$$C_{E,f}(\mathbf{r}_1, \mathbf{r}_2) \approx C_0 \exp \left[-\frac{ik_0(\mathbf{r}_1^2 - \mathbf{r}_2^2)}{2f} \right] \times \exp \left[\frac{-k_0^2 \sigma^2 (\mathbf{r}_1 + \mathbf{r}_2)^2}{16f^2} \right] \frac{J_1(k_c \Delta r/2)}{k_c \Delta r/2}. \quad (18)$$

Here $C_0 = k_0^2 E_0^2 D_L^2 \sigma^2 / 8f^2$ is the peak correlation amplitude, $\Delta r = |\mathbf{r}_1 - \mathbf{r}_2|$ is the relative position coordinate, and J_1 is a Bessel function of the first kind. The ratio

$$k_c = k_0 \frac{D_L}{f} \quad (19)$$

is a cutoff above which the PSD of the intensity

$$\rho_f(k) = C_0^2 \frac{2}{\pi k_c^2} \left[\cos^{-1} \left(\frac{k}{k_c} \right) - \frac{k}{k_c} \sqrt{1 - \frac{k^2}{k_c^2}} \right] \quad (20)$$

is strictly zero. Equation (20) is valid near the optical axis where $|\mathbf{r}_1|, |\mathbf{r}_2| \ll w(z)$.

D. Field and intensity probability distribution

In the previous sections, we focused on the average properties of speckle fields. Here we extend this discussion to predict the probability distribution of the electric-field strength $P(E)$ and intensity $P(I)$. Our approach focuses first on $P(E)$ and consists of two steps: (1) we find the regime where the central limit theorem applies, thereby assuring a Gaussian probability distribution; and (2) we identify $\langle E \rangle$ and $\langle E^2 \rangle$ as the lowest moments of the distribution, fully defining the Gaussian distribution.

We now interpret the electric field

$$E(\mathbf{r}; z) = \frac{-ik_0}{2\pi z} \int d^2 \mathbf{r}' E^-(\mathbf{r}') e^{-i\phi(\mathbf{r}')} e^{-k_0 |\mathbf{r} - \mathbf{r}'|^2/2z}$$

of Eq. (3) as a random variable constructed from a sum over incoherent complex phasors. The cross correlation function (CCF) $\langle E(\mathbf{r}_1; z) E(\mathbf{r}_2; 0) \rangle$ specifies the range over which the initial random field contributes to the final field. The closed-form expression for this CCF is similar to the field-field correlation function (8); the length scale for the decay of correlations $\sigma_{\text{CCF}}(z)$ again obeys Eq. (9), but with $M_{\text{CCF}}^2 = (1 + w^2/\sigma^2)^2$. When $w \gg \sigma$, i.e., the initial waist is much larger than the speckle size, the resulting Rayleigh range reduces to $z_{\text{R,CCF}} = k_0 \sigma^2/2$: as if each random source was

an individual Gaussian beam with extent σ . The criterion that a field $E(\mathbf{r}; z)$ have contributions from many incoherence sources is therefore $\sigma_{\text{CCF}}(z)/\sigma \gg 1$, i.e., $z \gg z_{\text{R,CCF}}$.

This identifies the central limit theorem's regime of applicability, and we now consider $E(\mathbf{r}; z)$ as a complex-valued Gaussian random variable. The probability distribution for the electric field is therefore a function of two independent degrees of freedom, here we select the quadrature variables E and E^* , giving $P(E, E^*)$. Most moments of this quantity are easy to identify using Eqs. (3), (4), (6), and (7): $\langle E \rangle = \langle E^2 \rangle = 0$, and similarly for E^* . Then Eq. (5) and the following discussion assure us that $\langle EE^* \rangle = \langle |E|^2 \rangle$ takes on a nonzero value. Together these fully define the Gaussian probability distribution for electric fields:

$$P(E, E^*) = \frac{1}{\pi \langle |E|^2 \rangle} \exp \left(-\frac{|E|^2}{\langle |E|^2 \rangle} \right), \quad (21)$$

and, using Eq. (13), the intensity distribution

$$P(I) = \frac{1}{\langle I \rangle} \exp \left(-\frac{I}{\langle I \rangle} \right), \quad (22)$$

follows directly. The intensity of a speckle field obeys an exponential distribution and the mean speckle intensity $\langle I \rangle$ should be equal to its standard deviation $(\langle I^2 \rangle)^{1/2}$.

E. Simulated speckle and the comparison with experiment

Having now fully set the stage for understanding and creating speckle laser beams, we turn to a laboratory confirmation of key prediction of these models relevant to cold atom experiments: the field-field correlation length C_E and the distribution of intensities $P(I)$.

In our laboratory, we directed a collimated laser beam (waist $w \approx 25$ mm) through a diffuser (divergence angle $\theta_d = 0.5^\circ$ and aperture $D = 20$ mm) focused immediately by a lens (focal length $f = 30$ mm), as depicted by Fig. 1 and quantified the optical speckle formed at the focal plane. We then imaged the optical speckle onto a charge coupled device (CCD) camera by using a Keplerian telescope with magnification $M = 46$. The CCD's 1024×1280 array of $4.8 \mu\text{m}$ pixels gave a $100 \mu\text{m} \times 130 \mu\text{m}$ magnified field of view with $0.1 \mu\text{m}$ pixels.

Our analytic results for C_E are valid in the Gaussian-beam limit ($w \ll D$) or uniform illumination limit ($w \gg D$). Because our experiment has $w \approx D$, we numerically simulated the optical speckle to compare with our measurements and both models.

For the numerical simulation, the desired optical speckle field $E_{i,j}$ is represented by a 1024×1280 array at the focal point of the lens. We use the optical Fourier transform property of lenses to compute this efficiently, whereby the field a focal distance beyond the lens is related to the Fourier transform of the field a focal distance prior to the lens (which we term the Fourier plane). An important aspect of this method is that the $0.1 \mu\text{m}$ grid spacing in the focal plane transforms to a 1.5 mm grid spacing in the Fourier plane.

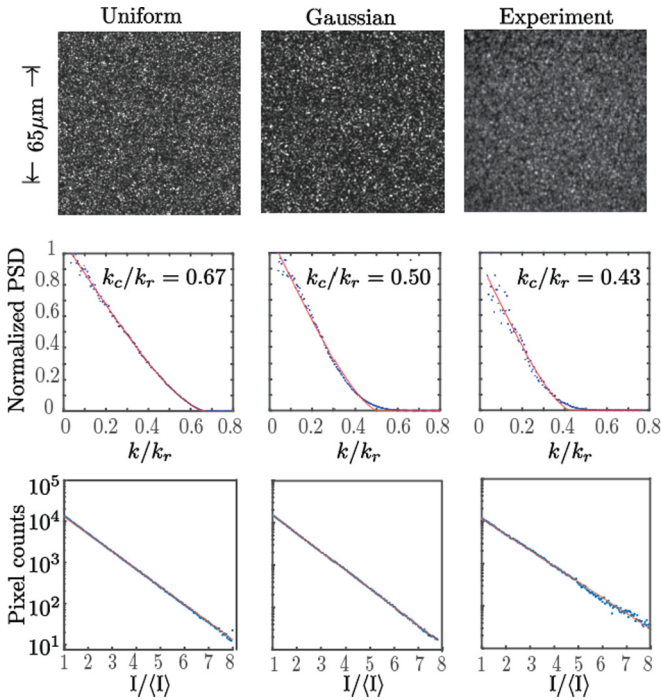


FIG. 2. Simulated and measured optical speckle. The columns in the figure correspond to simulated speckle with uniform laser beam, simulated speckle from a Gaussian laser beam and measured speckle. In each column, the first row shows the intensity of the optical speckle field. The second row shows the PSD of the intensity shown in the first row (symbols). The red curve shows a fit of Eq. (20) to the data, along with the resulting k_c . The third row histograms the intensity from the first row.

Our simulation progresses as follows: (1) We first initialize $E_{i,j}(z=0)$ to the field of either a uniform field or a Gaussian beam. (2) We then imprint random phases on each point.¹ (3) We set the field outside our physical aperture to zero. (4) Then we back-propagate the field to the Fourier plane and take the Fourier transform to obtain the field at the focal plane.

Figure 2 compares our measured speckle with numerics and our analytic model; the three columns depict the case of a uniformly illuminated aperture, Gaussian illumination, and experiment. The top row shows that intensity at the focal plane is qualitatively similar for all three cases. The middle row, the PSD (computed from the intensity in the top row, and plotted by blue symbols), highlights the differences. In each case, we fit Eq. (20) the PSD and extract k_c from the fits (red curves). Because Eq. (20) was derived for a uniformly illuminated aperture it provides a good fit to the uniform-illumination case but deviates at large k for Gaussian illumination and experiment. In contrast, the numerics for Gaussian illumination and the experiment are indistinguishable. In the bottom row, we histogram the intensity distribution and verify that in all three cases we recover the expected exponential falloff.

¹The grid size is much larger than the correlation length of the diffuser, so the imprinted phase at each grid point is uncorrelated with all other points.

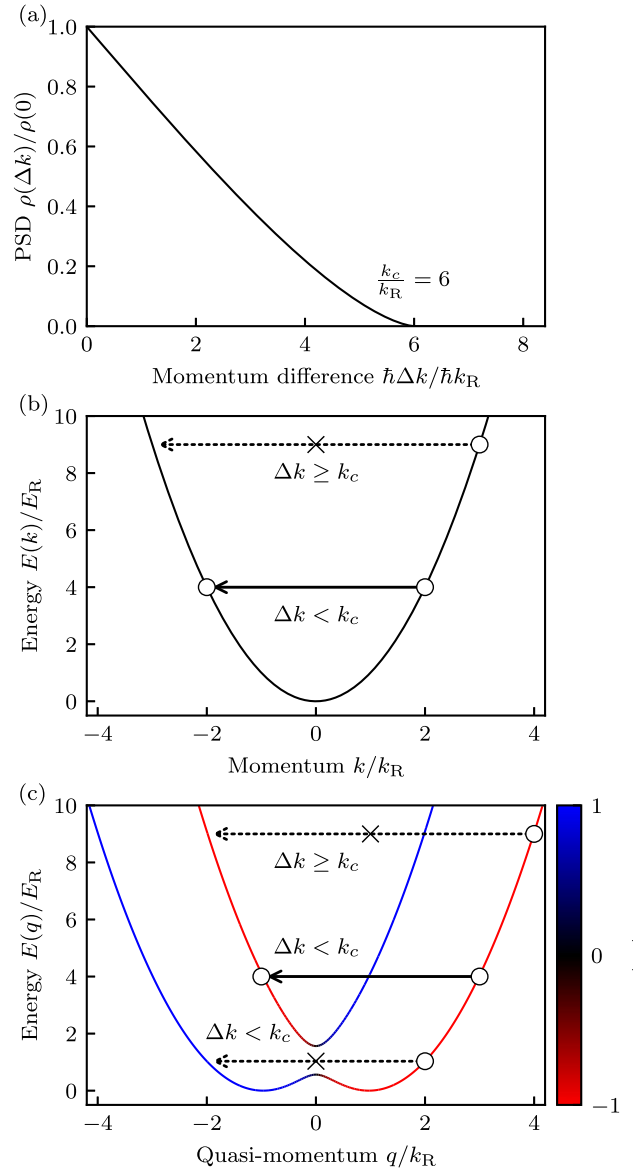


FIG. 3. Fermi's golden rule. Momentum is expressed in units of the single-photon recoil momentum k_R used to create SOC in panel (c). (a) Representative PSD for optical speckle with $k_c = 6k_R$. (b) Free particle dispersion relation. The dashed arrow marks the boundary above which the FGR rate vanishes, while the solid arrow provide an example with nonzero rate. (c) SOC dispersion relations computed for $\delta = 0$ add $\Omega_R = E_R$ colored according to the expectation value $\langle \sigma_z(q) \rangle$, with arrows marked as in panel (b). Note the transition through the gap in the dispersion relation at $E \approx E_R$ where the FGR rate is nearly zero.

III. SCATTERING OF A SPIN-ORBIT-COUPLED BEC FROM A SPECKLE POTENTIAL

We now focus on the motion of spin-orbit-coupled bosons in a speckle-induced disorder potential. In this section, we develop a Fermi golden rule (FGR) approach for scattering from a disorder potential both with and without SOC, as schematically depicted in Fig. 3. The first-order scattering processes captured by the FGR are possible when a matrix

element (here from the disorder potential) can couple energetically degenerate initial and final states (here momentum or quasimomentum states). We will see that the strength of this coupling is proportional to the PSD of the speckle potential, an example of which is shown in Fig. 3(a). As depicted in Fig. 3(b), this implies an absence of scattering for momenta differences larger than the speckle cutoff k_c . Adding SOC, as in Fig. 3(c), can suppress scattering for additional wave vectors. Because a spin-independent speckle potential has no spin-changing matrix element, the energetically allowed transition at an energy $E/E_R \approx 1$ between states of opposite spin is strongly suppressed. The following discussion quantifies these observations.

A. Fermi's golden rule

In this section we first develop our understanding of scattering from disorder potentials by deriving the FGR for spinless particles. With that understanding in hand we turn to the case adding SOC.

B. Spinless atoms

For spinless free particles, the unperturbed Hamiltonian $H = \hbar^2 k^2/2m$ implies that we study scattering between initial and final momentum states, labeled by $|k_0\rangle$ and $|k_f\rangle$, respectively. Figure 3(b) depicts examples by open circles, with arrows connecting initial states to final states.

The time evolution of the initial state $|\psi(0)\rangle = |k_0\rangle$ subject to the speckle potential $V(x)$ may always be expressed as

$$|\psi(t)\rangle = \sum_k C_{k,k_0}(t) e^{-i\omega_k t} |k\rangle, \quad (23)$$

with $C_{k,k_0}(0) = \delta_{k,k_0}$ and $\hbar\omega_k = \hbar^2 k^2/2m$. The coefficients $C_{k,k_0}(t)$ are governed by the time-dependent Schrödinger equation, giving the exact expression

$$C_{k_f,k_0}(t) = C_{k_f,k_0}(0) + \frac{1}{i\hbar} \sum_k \langle k_f | \hat{V} | k \rangle \int_0^t d\tau e^{i\omega_{k_f,k}\tau} C_{k,k_0}(\tau), \quad (24)$$

with

$$\omega_{k_f,k} = \omega_{k_f} - \omega_k \quad \text{and} \quad \hat{V} = \sum_x V(x) |x\rangle \langle x|. \quad (25)$$

An order-by-order perturbation theory is typically obtained by recursively inserting the integral expression for $C_{k_f,k_0}(t)$ back into the integrand; unfortunately, the general problem is intractable and we truncate the perturbation series at first order. This term is effectively obtained by replacing $C_{k_f,k_0}(\tau)$ with $C_{k_f,k_0}(0) = \delta_{k_f,k_0}$, giving

$$C_{k_f,k_0}(t) = \delta_{k_f,k_0} + \frac{1}{i\hbar} \int_0^t d\tau \langle k_f | \hat{V} | k_0 \rangle e^{i\omega_{k_f,k_0}\tau}. \quad (26)$$

Unfortunately, we do not know $V(x)$ for any specific realization of the speckle potential.

In Sec. II we characterized optical speckle in terms of second-order statistical metrics such as the PSD, here equal to $\rho(k_f - k_0) = \langle \langle k_f | \hat{V} | k_0 \rangle \langle k_0 | \hat{V} | k_f \rangle \rangle$, where the double brackets indicate the ensemble average. The resulting

ensemble-averaged transition probability

$$P_{k_f,k_0}(t) = \frac{\rho(k_f - k_0)}{\hbar^2} \left[\frac{2}{\omega_{k_f,k_0}} \sin \left(\frac{\omega_{k_f,k_0} t}{2} \right) \right]^2 \quad (27)$$

is a sharply peaked function centered at $\omega_{k_f,k_0} = 0$ with width $2\pi/t$, showing that a narrow range of energy-matching states can be populated. For long times $\omega_{k_f,k_0} t \gg 1$, the quantity in square brackets converges to a scaled Dirac δ function $t\delta(\omega_{k_f,k_0})$.

Figure 3(a) displays the normalized PSD for a speckle potential computed with $k_c = 6k_R$, reminding us that $\rho(k) = 0$ for $k \geq k_c$. Our FGR expression allows two types of scattering processes for the free particle dispersion shown in Fig. 3(b). In the first process, depicted by the black arrow, the atom's initial momentum is reversed, changed by $\Delta k = 2k_0$; as indicated by the dashed line, this process is second-order forbidden for $k_0 \geq k_c/2$. In the second process (not pictured), the atom's momentum is only infinitesimally changed: spreading the wave-packet, but leaving the average momentum unchanged. This picture shows that backscattering is essential for momentum relaxation.

C. Spin-orbit-coupled atoms

Our 1D SOC coupling [8] is created by illuminating a two-level atom with a pair of counterpropagating lasers with wavelength λ_R tuned to drive stimulated Raman transitions between states $\{|q + k_R, \uparrow\rangle, |q - k_R, \downarrow\rangle\}$. Here $\hbar k_R = 2\pi\hbar/\lambda_R$ and $E_R = \hbar^2 k_R^2/2m$ are the single-photon Raman recoil momentum and energy, respectively. Subject to this Raman coupling, the atoms obey the 1D Hamiltonian

$$\hat{H}(q) = \frac{\hbar^2}{2m} (q\hat{1} + k_R\hat{\sigma}_z)^2 + \frac{\delta}{2}\hat{\sigma}_z + \frac{\hbar\Omega_R}{2}\hat{\sigma}_x, \quad (28)$$

where $\{\hat{1}, \hat{\sigma}_x, \hat{\sigma}_y, \hat{\sigma}_z\}$ are the identity and Pauli operators, respectively. Here q is the quasimomentum, Ω_R is the Raman coupling strength, and δ is the detuning from the two-photon Raman resonance condition. The resulting dispersion relations, plotted in Fig. 3 for $\delta = 0$ and $\Omega_R = E_R$, have energies $E^\pm(q)$ labeled by q along with \pm to indicate if they are in the upper or lower band.

These new energies and their associated amplitudes

$$|q, \pm\rangle \propto a_\pm(q) |q - k_R, \downarrow\rangle + b_\pm(q) |q + k_R, \uparrow\rangle$$

change the potential scattering processes, which we again compute by using a FGR expression. The coefficients

$$a_\pm(q) = \pm \frac{\Omega_R}{2} \quad \text{and} \quad b_\pm(q) = \pm \frac{\Delta(q)}{2} + \frac{\sqrt{\Delta^2(q) + \Omega_R^2}}{2}$$

along with the quasimomentum-dependent detuning

$$\Delta(q) = \frac{2\hbar^2 q k_R}{m} + \delta \quad (29)$$

fully define these superposition states.

Following the same FGR argument presented above for initial states $|q_0, -\rangle$ in the lower dispersion scattering from

a spin-independent speckle potential, we find scattering probabilities

$$P_{q_f, q_0}^{\pm}(t) = \frac{\rho(\Delta q)}{\hbar^2} \left| \frac{2 \sin(\omega_{q_f, q_0}^{\pm} t)}{\omega_{q_f, q_0}^{\pm}} \langle q_f, \pm | e^{i\Delta q x} | q_0, - \rangle \right|^2 \quad (30)$$

expressed in terms of the quasimomentum and energy differences $\hbar\Delta q = \hbar q_f - \hbar q_0$ and $\hbar\omega_{q_f, q_0}^{\pm} = E^{\pm}(q_f) - E^{\pm}(q_0)$. For most initial states $|q_0, -\rangle$, such as the two higher-energy states marked in Fig. 3(c), the scattering is essentially unchanged from our spinless example, with scattering occurring between energy-matched states with the same initial and final spin. In contrast, for initial states residing in the SOC energy gap there is no energy-matched state of the same spin available for backscattering; as indicated by the dashed line, scattering is greatly suppressed. We note that backscattering is not completely blocked because the energy matching states $|\pm q_0, -\rangle$ are not spin eigenstates and do have some spin overlap.

D. Computed scattering rates

We now use these FGR expressions to compute the scattering rates for both forward-scattering and backscattering processes. Because we are interested in transport properties, we define forward-scattering processes as those that leave the sign of the group velocity unchanged and backscattering processes and those that reverse the direction of motion. We therefore consider initial states $|q_0, -\rangle$ in the lower band with positive group velocity. Because the lower energy SOC dispersion plotted in Fig. 4 can have a pair of minima located at $\pm q_{\min}$, we always select $q_0 > q_{\min}$ to assure positive group velocity. We numerically evaluated the FGR for ^{87}Rb atoms illuminated with $\lambda_R = 790$ nm Raman lasers, giving $E_R = \hbar \times 3.7$ kHz, and for speckle with $k_c = 6k_R$. The $t = 13.4$ ms interaction time was selected to be experimentally relevant.

The right panels of Fig. 4 show the normalized scattering rate computed for four different values of Ω_R , with the backscattering rate plotted in black and forward scattering plotted in red. These rates combine the contributions from the \pm bands in Eq. (30).

Figure 4(a), computed for $\Omega_R = 0$ (equivalent to the case with no SOC), shows two key effects. First, the diverging forward- and back-scattering rates at low energy follow from the diverging density of states (DoS) in 1D. Second, the rate of backscattering (black) falls to zero when $\delta q > k_c$, while forward scattering (red) simply falls with the DoS. Figures 4(b) and 4(c) show cases with a well-resolved SOC energy gap. As expected, backscattering is nearly completely suppressed for initial energies in the energy gap, while forward scattering is hardly changed. In addition, a pair of singular features border of the energy gap, resulting from the diverging DoS and the local extrema of the dispersions. Figure 4(d) shows the same phenomena, but just as the two minima at $\pm q_{\min}$ have merged into a single minimum at $q_{\min} = 0$.

We therefore conclude, for noninteracting particles backscattering and momentum relaxation is nearly completely suppressed for atoms starting in the SOC energy gap.

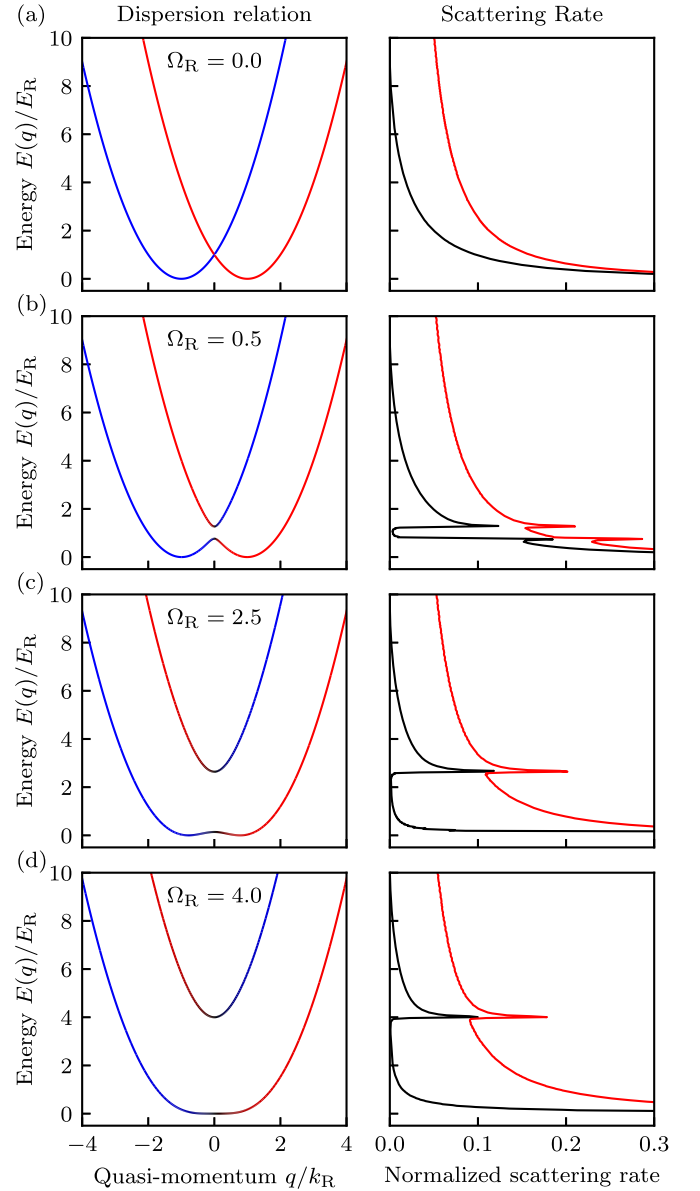


FIG. 4. Fermi's golden rule scattering rate for $\Omega_R/E_R = 0, 0.5, 2.5,$ and 4.0 . Left column shows SOC dispersion relations computed for each Ω_R , colored as in Fig. 3. Right column shows normalized scattering rate as a function of initial energy for the initial state $|q_0, -\rangle$ with $q_0 \geq q_{\min}$, i.e., in the bottom dispersion and to the right of the higher momentum local energy minimum. The backscattering rate is plotted in black and the forward scattering plotted in red.

IV. NUMERICAL SIMULATION OF GROSS-PITAEVSKII EQUATIONS

Our single-particle FGR results only describe the short-time scattering from a disorder potential; they cannot describe the full approach to equilibrium. To bridge the gap between the FGR and the physical system, we need to account for both higher-order scattering processes and interparticle interactions. In our proposed SOBEC realization, all aspects of the SOC Hamiltonian and the speckle potential are tunable, making SOBECs an ideal system for exploring enhanced transport in 1D quantum wires.

A. Gross-Pitaevskii equations

Here we numerically study the deceleration of a SOBEC initially moving in a speckle potential by using the time-dependent Gross-Pitaevskii equation (GPE). The time-dependent GPE

$$i\hbar\partial_t\Psi(\mathbf{r},t) = \left[-\frac{\hbar^2}{2m}\nabla^2 + V(\mathbf{r}) + g_{3D}|\Psi(\mathbf{r},t)|^2 \right] \Psi(\mathbf{r},t) \quad (31)$$

is a nonperturbative dynamical description [13] of a large number of interacting identical bosons occupying the same spatial mode $\Psi(\mathbf{r},t)$ normalized to the total atom number $N = \int d^3\mathbf{r}|\Psi(\mathbf{r},t)|^2$. The interaction strength $g_{3D} = 4\pi\hbar^2 a_s/m$ can be expressed in terms of the s -wave scattering length a_s . This GPE provides a good description of low-temperature spin-polarized BECs, with negligible thermal excitations [14].

Since our focus is on 1D transport, we must first obtain a 1D description of our 3D system [15]. Here we assume that the potential $V(\mathbf{r}) = V(x) + V_\perp(y,z)$ can be separated into a weak longitudinal potential $V_\parallel(x)$ along with a strongly confining transverse potential $V_\perp(y,z)$. When the single-particle energy spacing from $V_\perp(y,z)$ greatly exceeds all other energy scales, the 3D wave function can be factorized into

$$\Psi(\mathbf{r},t) = \psi(x,t)\phi(y,z), \quad (32)$$

containing a longitudinal term of interest giving the 1D density $n(x) = |\psi(x,t)|^2$, and a transverse term $\phi(y,z)$, normalized to unity, assumed to be the ground state of the transverse potential. Inserting this ansatz into the GPE and integrating out the transverse degrees of freedom gives the 1D GPE:

$$i\hbar\partial_t\psi = \left[-\frac{\hbar^2}{2m}\partial_x^2 + V(x) + g|\psi|^2 \right] \psi, \quad (33)$$

which is suitable for studying single-component 1D bosons in a speckle potential with the 1D interaction strength

$$g = g_{3D} \int dydz |\phi(y,z)|^4. \quad (34)$$

For compactness of notation here and below, we omit the functional dependence of ψ on x and t .

The two-component 1D spinor GPE describing SOBECs extends Eq. (28) to include interactions and consists of a pair of coupled nonlinear differential equations:

$$i\hbar\partial_t\psi_\uparrow = \left[\frac{\hbar^2}{2m}(-i\partial_x + k_R)^2 + \frac{\delta}{2} + V(x) + g_{\uparrow\uparrow}|\psi_\uparrow|^2 + g_{\uparrow\downarrow}|\psi_\downarrow|^2 \right] \psi_\uparrow + \frac{\Omega_R}{2}\psi_\downarrow, \quad (35)$$

$$i\hbar\partial_t\psi_\downarrow = \left[\frac{\hbar^2}{2m}(-i\partial_x - k_R)^2 - \frac{\delta}{2} + V(x) + g_{\downarrow\downarrow}|\psi_\downarrow|^2 + g_{\uparrow\downarrow}|\psi_\uparrow|^2 \right] \psi_\downarrow + \frac{\Omega_R}{2}\psi_\uparrow, \quad (36)$$

including the interaction strengths $g_{\uparrow\uparrow}$, $g_{\uparrow\downarrow}$, and $g_{\downarrow\downarrow}$. Here we focus on the specific case of ^{87}Rb atoms [16] in the $F=1$ ground state manifold and have selected $|\uparrow\rangle = |m_F=0\rangle$ and $|\downarrow\rangle = |m_F=-1\rangle$. The interactions can be parametrized

TABLE I. Simulation parameters

Description	Symbol	Value
^{87}Rb atomic mass	m	1.42×10^{-25} kg
Raman laser wavelength	λ_R	790 nm
Recoil energy	E_R	$\hbar \times 3.678$ kHz
Dipole trap frequency	$\omega/2\pi$	10 Hz
Angle of Raman beams	θ_R	180°
Speckle potential cutoff	k_c	$6k_R$
Average speckle potential	$\langle V(x) \rangle$	$0.05E_R$
Grid spacing	δx	66 nm
Grids points (single-component)	N_x	$2^{14} + 1$
Grids points (SOC)	N_x	$2^{13} + 1$
Atom number	N	2×10^5
Chemical potential	μ	$\hbar \times 300$ Hz

in terms of an s -wave pseudopotential $(g_{0,3D} + g_{2,3D}\vec{F}_\alpha \cdot \vec{F}_\beta)\delta(\mathbf{r}_i - \mathbf{r}_j)$ now dependent on spin. In ^{87}Rb 's $F=1$ manifold $g_{0,3D} = 100.86 \times 4\pi\hbar^2 a_B/m$ is vastly larger than $g_{2,3D} \approx -4.7 \times 10^{-3} \times g_{0,3D}$, where a_B is the Bohr radius [17,18]. The interaction coefficients reduce to effective 1D interaction strengths just as in the single-component case and are related to the generic coefficients [19,20] via $g_{\uparrow\uparrow} = g_0$ and $g_{\downarrow\downarrow} = g_{\uparrow\downarrow} = g_0 + g_2$. Table I summarizes the parameters used in our simulations.

Our simulation results are divided into two sections: Sec. IV B hones our understanding by considering a single-component BEC evolving in a speckle potential, and then in Sec. IV C we contrast with the case with SOC. In both sections, we simulate initially trapped BECs accelerated to an initial momentum k_0 or quasimomentum q_0 and we study their deceleration. All the results are averaged over 20 speckle realizations, as in Fig. 2(b). The average speckle potential $\hbar \times 200$ Hz $\approx 0.05E_R$ was selected to be weak enough to cause no trapping effect yet strong enough to produce significant deceleration within 15 ms.

B. Single-component systems

The simulations are performed in three steps to model as accurately as possible a realistic experimental sequence. First, we initialize a ground-state BEC in a harmonic trap by using imaginary time evolution [21], giving the density distribution plotted in black in Fig. 5(a), and follow with real-time evolution. Second, because the BEC's narrow momentum distribution is centered at $k=0$, we briefly apply a linear potential αx with time-evolution approximately described by the phase factor $\exp(ik_0x)$, a momentum translation operator that transforms $|k=0\rangle$ to $|k_0\rangle$. Third, having prepared our $|k_0\rangle$ initial state, we replace the harmonic potential with a speckle potential (with $k_c/k_R = 6$) and follow the time evolution for 16 ms. Figure 5(b) captures the main result of this section: when $k_0 > k_c/2$ the time-evolution is almost unchanged by the speckle potential, while slowly moving initial states are both decelerated and exhibit considerable interference.

Figure 5(c) plots the ensemble-averaged momentum $\langle k(t) \rangle$ as a function of time for a range of initial states with k_0 from near zero to $k_0/k_R = 3.3$, and Fig. 5(d) plots the final momentum k_f as a function of k_0 . At $t=0$, the average

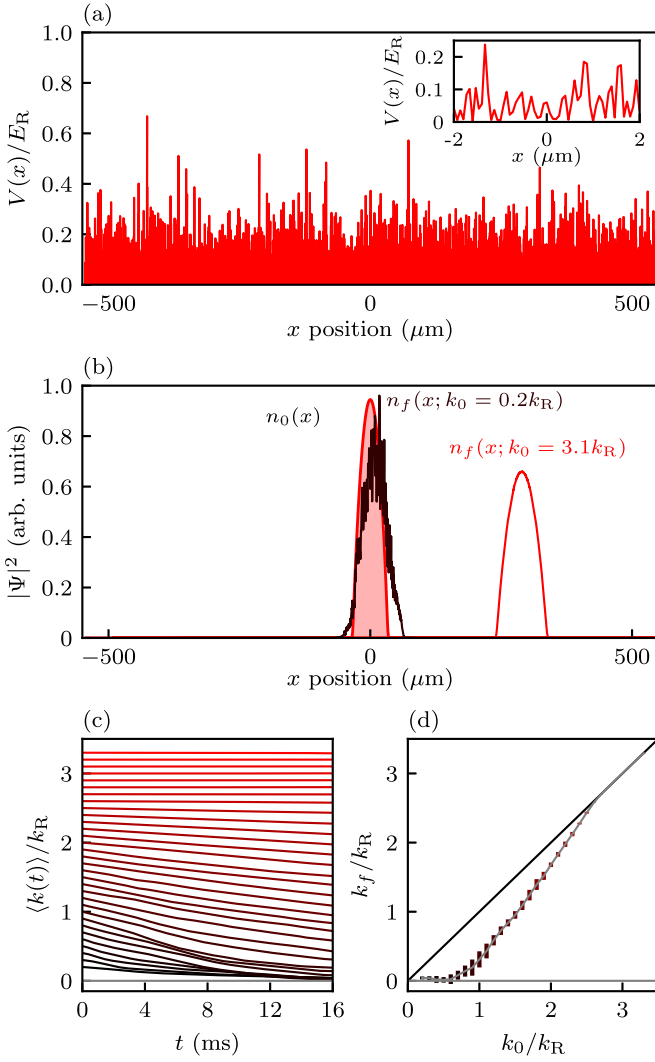


FIG. 5. Single-component GPE simulation with $k_c/k_R = 6$. (a) Representative disorder potential. The red curve plots a representative speckle potential used in our simulations. The inset shows an expanded view with visible structure. (b) Density distributions. The filled red curve depicts the initial density distribution, while the black and red curves show the final-state density distributions for initial momenta $|k_0 = 0.2k_R$ and $|k_0 = 3.1k_R$, above and below $k_c/2$, respectively. (c) Mean momentum. $\langle k(t) \rangle$ averaged over 20 speckle realizations is plotted for a range of initial momentum in the range of 0 to $3.3k_R$, the $t = 0$ point of each curve marks the initial k_0 . (d) Deceleration. The colored symbols plot $k_f = \langle k(t = 16 \text{ ms}) \rangle$ as a function of k_0 along with their standard deviations, and the black line marks $k_f = k_0$, corresponding to ballistic motion.

momentum is $\langle k(t) \rangle = k_0$; for $k_0 \gtrsim k_c/2$ the BEC evolves ballistically, leaving $\langle k(t) \rangle$ unchanged, while $\langle k(t) \rangle = k_0$ falls rapidly for smaller k_0 . Both of these observations are consistent with our FGR analysis which showed a complete absence of momentum-changing backscattering for $k_0 \geq k_c/2$, and with rapidly increasing backscattering as k falls to zero.

C. Spin-orbit-coupled BECs

As in the single-component case, simulations with SOC begin with three steps aligned with experiment; however, the

process of preparing the initial quasimomentum state $|q_0, -\rangle$ is considerably more elaborate than preparing a momentum state $|k_0\rangle$ in a single-component system. (1) As before, we initialize a ground-state BEC in a harmonic trap by using imaginary time evolution, spin polarized in state $|k_0 = 0, \downarrow\rangle$. (2) We then use a combination of adiabatic and unitary evolution (described below) to transform this state into $|q_0, -\rangle$ for $\delta = 0$ and Ω_R ranging from $0.5E_R$ to $8E_R$. (3) Lastly, we remove the harmonic potential and again follow the time evolution with a speckle potential ($k_c/k_R = 6$) for 16 ms.

Our procedure (2) begins with the observation that, in a frame moving with velocity $\hbar\delta k/m$, the detuning δ present SOC Hamiltonian in Eq. (28) is Doppler shifted [22,23] to $\delta + 2\hbar^2\delta k k_R/m$. Our first task is to adiabatically transform the initial state $|k_0 = 0, \downarrow\rangle$ into $|q_{\min}, -\rangle$, a ground state SOBEC with quasimomentum centered at $q = q_{\min}$, the global minima of the SOC dispersion, but with $\delta = 2\hbar^2(q_0 - q_{\min})k_R/m$. We achieve this by ramping up the Raman coupling strength from zero to Ω_R on a timescale slow compared with $\hbar/\Delta(q_0)$. In the slow ramp-up process, the harmonic trap provides the restoring force required to keep the state at a local minima of the dispersion [8], i.e., with zero group velocity. Lastly, we diabatically set $\delta = 0$ and apply momentum kick $\exp[i(q_0 - q_m)x]$, giving the desired state $|q_0, -\rangle$.

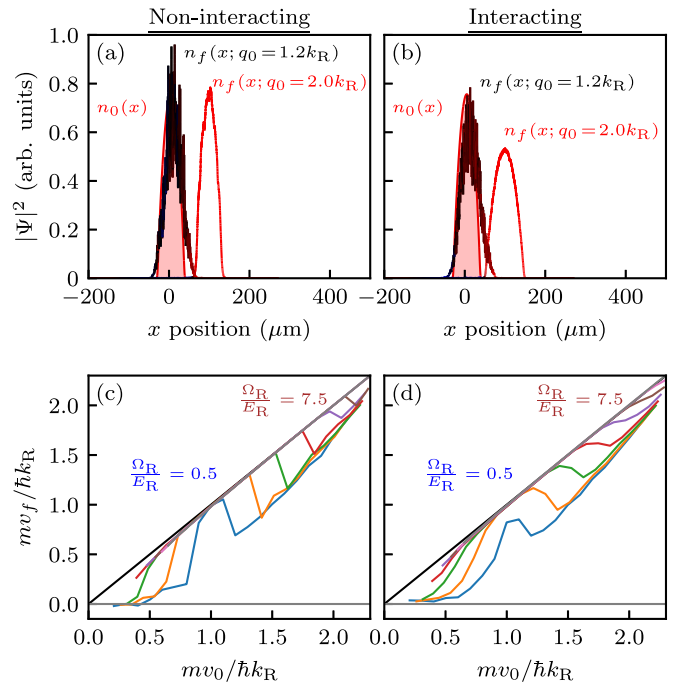


FIG. 6. Motion in the presence of speckle and SOC. The left column was computed without interactions and the right column added interactions. (a), (b) Density distributions colored by their magnetization according to the color bar in Fig. 3. The shaded curve depicts the initial density distribution, while the remaining red and black curves were computed for $q_0 = 2.0k_R$ (in the SOC gap) and $q_0 = 1.2k_R$ (below the SOC gap), respectively. (c), (d) Ensemble averaged final group velocity plotted as a function of initial group velocity for coupling strengths from $0.5E_R$ to $7.5E_R$, spaced by $1.0E_R$. The results in panels (c) and (d) were averaged over 20 random speckle realizations.

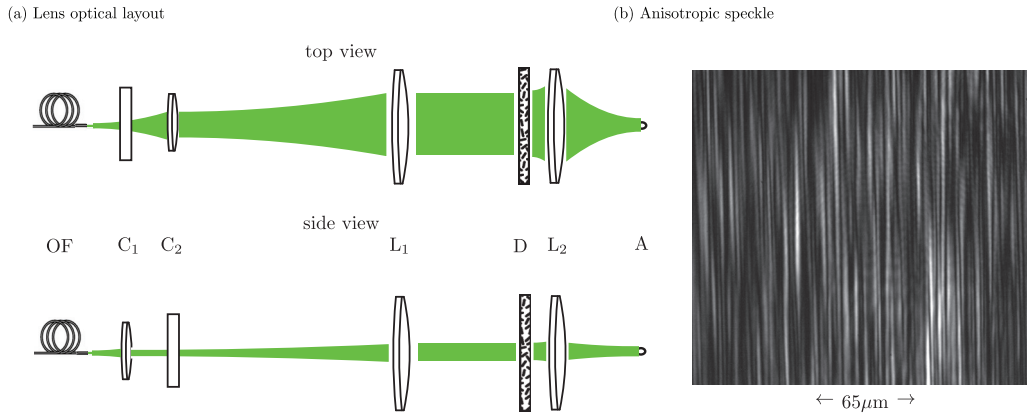


FIG. 7. Optical design. (a) The design of optics viewed in two directions. OF denotes optical fiber. Lenses C_1 and C_2 are cylindrical lenses: C_1 focuses the beam in the vertical direction, and C_2 focuses the beam in the horizontal direction. L_1 is a spherical lens that collimates the beam. D is the optical diffuser that imprints a random phase on the beam. L_2 is an aspherical lens that focuses the beam to the atoms labeled with A. (b) Experimental image of optical speckle with anisotropic correlation length.

Figures 6(a) and 6(b) show representative density distributions $n(x) = |\psi_\uparrow(x, t)|^2 + |\psi_\downarrow(x, t)|^2$ before and after a 16 ms time evolution with $\Omega_R = 2E_R$, both Fig. 6(a) with no interactions and Fig. 6(b) with interactions. In both cases the pink shaded curve depicts the initial density distribution, while the density distributions for initial quasimomenta of $q_0 = 1.2k_R$ and $2.0k_R$ are shown by the black and red curves, respectively. In both cases the momentum exchange for backscattering is below k_c ; however, as with the FGR results, these direct simulations show that initial states prepared with energy within the SOC energy gap experience negligible change in velocity, independent of the presence of interactions.

While the free particle group velocity is simply related to the wave vector by $v = \hbar k/m$, atoms evolving according to the SOC dispersions, as in Fig. 4, have their group velocity given by the more complex relation

$$\frac{v_\pm}{v_R} = \frac{q}{k_R} \left\{ 1 \pm \left[\left(\frac{q}{k_R} \right)^2 + \left(\frac{\Omega_R}{4E_R} \right)^2 \right]^{-1/2} \right\}, \quad (37)$$

for atoms in state $|q, \pm\rangle$, expressed in units of the recoil velocity $v_R = \hbar k_R/m$. Because we are interested in transport phenomena, it is this group velocity, not the quasimomentum, that is the quantity of primary interest.

Figures 6(c) and 6(d) plot the final group velocity v_f as a function of initial group velocity v_0 after a 16 ms period of free evolution, both Fig. 6(c) with no interactions and Fig. 6(d) with interactions, and with Ω_R from $0.5E_R$ to $7.5E_R$. As compared with the simulations without SOC in Fig. 5(d), these curves show a near-complete suppression of relaxation for velocities near $v_0 \approx v_R$, in the SOC energy gap, and with an increasing window of suppression with increasing Ω_R .

Lastly, we see that interaction effects do play a role, leading to more rapid deceleration. The origin of this effect can be understood by comparing the red curves in Figs. 6(a) and 6(b): adding interactions leads a mean-field driven expansion of the BEC, increasing the range of velocities present. As a result, when the SOC energy gap is small (small Ω_R), a significant fraction of the BEC's velocity distribution falls outside the

SOC energy gap, thereby sampling points in the dispersion where first-order backscattering is allowed. At larger Ω_R , motion is near ballistic near the center of the SOC gap, but the transition from ballistic to decelerated is smoothed as compared with the case with no interactions.

V. CONCLUSION

Our analytical and numerical studies of the transport of SOBECs in disorder potentials clearly show dramatically enhanced transport for initial states in the SOC energy gap. The enhanced transport described here results from the same physics giving rise to a spin transistor in Ref. [24], which also relied on a combination of kinematic and matrix-element effects to yield nonreciprocal-appearing transport behavior. In the Appendix, we describe an explicit experimental proposal using laser speckle derived from a 532 nm green laser and an off-the-shelf optical diffuser. In this proposal, SOC is generated from a pair of 790 nm laser beams intersecting at the atoms, and initial states would be prepared as described above. The protection from backscattering is independent of quantum statistics: noninteracting fermions would experience a conductivity increased by the factor predicted by the FGR when the Fermi energy resides in the SOC gap. As with the interacting SOBEC we analyzed, we expect that fermionic systems with moderate interactions would show gains in conductivity; however, the details of this latter case would necessitate future study. More speculatively, strongly interacting systems of 1D bosons or fermions—for example confined in a two-dimensional (2D) optical lattice of 1D tubes—with disorder and SOC would be a new system to study many-body localization [25].

Reference [26] showed that, in lattices, the type of 1D SOC in Eq. (28) has the same dispersion as the edge modes of 2D Z_2 topological insulators [27]. Together with our finding, this indicates that 1D nanowires with SOC either of the Rashba [28] or linear-Dresselhaus [29] type should provide the same protection to backscattering from spin-independent disorder as would be observed at the edge of a topological insulators.

ACKNOWLEDGMENTS

This work was partially supported by the AFOSRs Quantum Matter MURI, NIST, and the NSF through the PFC at the JQI. We benefited from laboratory assistance from E. M. Altuntas, C. J. Billington, and F. Salces-Carcoba. We are grateful for the meticulous reading of our paper by the aforementioned individuals along with W. McGehee and G. H. Reid. Also thanks to B. Shapiro for catching a typographical error and suggesting references in the preprint stage.

APPENDIX: SPECKLE-BEAM DESIGN FOR SPIN-ORBIT-COUPLING EXPERIMENTS

In practice, the speckle beam must satisfy two requirements: The first is anisotropic field-field correlation length: small along \mathbf{e}_x and large along \mathbf{e}_y and \mathbf{e}_z so that scattering occurs predominantly along \mathbf{e}_x . The second is that the beam width along \mathbf{e}_x should uniformly illuminate the elongated atomic ensemble (with expected diameter of about $50 \mu\text{m}$). To observe the effect of SOC-suppressed transport, the speckle potential must couple energy matched states across the SOC gap, shown by the dashed line in Fig. 3(c). This implies PSD of speckle potential along \mathbf{e}_x satisfies $k_c \gtrsim 4k_R$, informing the selection of beam-size and lenses. The requirement that the correlation length along \mathbf{e}_y be large implies that at

the diffuser plate, the beam be much smaller along \mathbf{e}_y than along \mathbf{e}_x .

To satisfy these joint requirements, we created the speckle beam shown in Fig. 7(a), that begins with a 532 nm laser beam emanating from an optical fiber. The beam out of an optical fiber travels through the cylindrical lens C_1 (focusing along \mathbf{e}_y) before encountering a cylindrical lens C_2 (focusing along \mathbf{e}_x) as shown in Fig. 7(a), given more rapid divergence along \mathbf{e}_x than \mathbf{e}_y . The beam is then collimated by L_1 , a $f = 250$ mm spherical lens, giving a beam width of around 25 mm along \mathbf{e}_x and less than $500 \mu\text{m}$ along \mathbf{e}_y (on the same scale as the diffuser plate's correlation length).

The beam then traverses the diffuser plate (Edmund Optics² part number #47-680, with divergence angle $\theta_d = 0.5^\circ$) and is focused by L_2 , a $f = 30$ mm lens. Figure 7(b) shows a test image of speckle beam at the focal plane, its intensity correlation length is less than $0.5 \mu\text{m}$ along \mathbf{e}_x and about $10 \mu\text{m}$ along \mathbf{e}_y . The beam widths along both directions are about $250 \mu\text{m}$.

²Certain commercial equipment, instruments, or materials are identified in this paper in order to specify the experimental procedure adequately. Such identification is not intended to imply recommendation or endorsement by the National Institute of Standards and Technology, nor is it intended to imply that the materials or equipment identified are necessarily the best available for the purpose.

-
- [1] P. W. Anderson, *Phys. Rev.* **109**, 1492 (1958).
 [2] D. S. Wiersma, P. Bartolini, A. Lagendijk, and R. Righini, *Nature (London)* **390**, 671 (1997).
 [3] F. Scheffold, R. Lenke, R. Tweer, and G. Maret, *Nature (London)* **398**, 206 (1999).
 [4] M. Störzer, P. Gross, C. M. Aegerter, and G. Maret, *Phys. Rev. Lett.* **96**, 063904 (2006).
 [5] L. Sanchez-Palencia, D. Clément, P. Lugan, P. Bouyer, G. V. Shlyapnikov, and A. Aspect, *Phys. Rev. Lett.* **98**, 210401 (2007).
 [6] J. Billy, V. Josse, Z. Zuo, A. Bernard, B. Hambrecht, P. Lugan, D. Clément, L. Sanchez-Palencia, P. Bouyer, and A. Aspect, *Nature (London)* **453**, 891 (2008).
 [7] G. Roati, C. D'Errico, L. Fallani, M. Fattori, C. Fort, M. Zaccanti, G. Modugno, M. Modugno, and M. Inguscio, *Nature (London)* **453**, 895 (2008).
 [8] Y.-J. Lin, K. Jimenez-Garcia, and I. B. Spielman, *Nature (London)* **471**, 83 (2011).
 [9] D. Clément, A. F. Varón, J. A. Retter, L. Sanchez-Palencia, A. Aspect, and P. Bouyer, *New J. Phys.* **8**, 165 (2006).
 [10] B. Shapiro, *J. Phys. A: Math. Theor.* **45**, 143001 (2012).
 [11] J. W. Goodman, *Speckle Phenomena in Optics: Theory and Applications* (Roberts and Company Publishers, Englewood, CO, 2007).
 [12] S. A. Self, *Appl. Opt.* **22**, 658 (1983).
 [13] L. Erdős, B. Schlein, and H.-T. Yau, *Ann. Math.* **172**, 291 (2010).
 [14] F. Dalfovo, S. Giorgini, L. P. Pitaevskii, and S. Stringari, *Rev. Mod. Phys.* **71**, 463 (1999).
 [15] W. Bao, D. Jaksch, and P. A. Markowich, *J. Comput. Phys.* **187**, 318 (2003).
 [16] Y. Kawaguchi and M. Ueda, *Phys. Rep.* **520**, 253 (2012).
 [17] E. G. M. van Kempen, S. J. J. M. F. Kokkelmans, D. J. Heinzen, and B. J. Verhaar, *Phys. Rev. Lett.* **88**, 093201 (2002).
 [18] A. Widera, F. Gerbier, S. Fölling, T. Gericke, O. Mandel, and I. Bloch, *New J. Phys.* **8**, 152 (2006).
 [19] T.-L. Ho, *Phys. Rev. Lett.* **81**, 742 (1998).
 [20] T. Ohmi and K. Machida, *J. Phys. Soc. Jpn.* **67**, 1822 (1998).
 [21] M. L. Chiofalo, S. Succi, and M. P. Tosi, *Phys. Rev. E* **62**, 7438 (2000).
 [22] L. W. Cheuk, A. T. Sommer, Z. Hadzibabic, T. Yefsah, W. S. Bakr, and M. W. Zwierlein, *Phys. Rev. Lett.* **109**, 095302 (2012).
 [23] A. Valdés-Curiel, D. Trypogeorgos, E. E. Marshall, and I. B. Spielman, *New J. Phys.* **19**, 33025 (2017).
 [24] M. E. Mossman, J. Hou, X.-W. Luo, C. Zhang, and P. Engels, *Nat. Commun.* **10**, 3381 (2019).
 [25] D. A. Abanin, E. Altman, I. Bloch, and M. Serbyn, *Rev. Mod. Phys.* **91**, 021001 (2019).
 [26] D. Hügél and B. Paredes, *Phys. Rev. A* **89**, 023619 (2014).
 [27] C. L. Kane and E. J. Mele, *Phys. Rev. Lett.* **95**, 146802 (2005).
 [28] Y. A. Bychkov and E. I. Rashba, *J. Phys. C: Solid State Phys.* **17**, 6039 (1984).
 [29] G. Dresselhaus, *Phys. Rev.* **100**, 580 (1955).